Water Air Soil Pollut (2025) 236:866
https://doi.org/10.1007/s11270-025-08462-5

Green $MnFe_2O_4$/g-C_3N_4 Nanoparticles for Pb(II) Treatment in Contaminated Water: Experimental Insights and Machine Learning Integration

Saba Madadgar · Faramarz Doulati Ardejani · Zohreh Boroumand · Christoph Butscher · Reza Taherdangkoo

Received: 17 March 2025 / Accepted: 4 August 2025 / Published online: 3 October 2025
© The Author(s) 2025

Abstract This study evaluates the effectiveness of $MnFe_2O_4$/g-C_3N_4 spinel ferrites nanoparticles, synthesized using Chrysopogon zizanioides root powder, in removing Pb (II) ions from contaminated water through the adsorption process. The nanoparticles were synthesized using the co-precipitation method. Firstly, the CZ/$MnFe_2O_4$/g-C_3N_4 nanoparticles (CZMNCN) were characterized using various techniques such as Fourier-transform infrared spectroscopy (FTIR), field emission scanning electron microscopy (FE-SEM), energy-dispersive X-ray spectroscopy (EDS), Brunauer–Emmett–Teller (BET) surface area analysis, dynamic light scattering (DLS), zeta potential measurement, Raman spectroscopy (RAMAN), and vibrating sample magnetometry (VSM). The analyses confirmed the successful synthesis and the magnetic properties of the nanosorbent. The adsorption capacity of the CZ/$MnFe_2O_4$/g-C_3N_4 nanoparticles was then tested, demonstrating a high removal efficiency for Pb (II) from contaminated water. The effects of various parameters on the adsorption process, including pH, adsorbent dosage, contact time, initial Pb (II) concentration, and temperature, were investigated. Kinetic studies revealed that the adsorption process followed a pseudo-second-order model with a coefficient of determination of 97.32%, indicating a strong correlation. Additionally, the Freundlich isotherm model best described the adsorption of Pb (II) by the nanoparticles. Thermodynamic studies indicated that the adsorption of Pb (II) was an endothermic and spontaneous process. The study also examined the desorption capability and reusability of the nanosorbent over multiple cycles, finding that it could be effectively regenerated and reused, with a high percentage of recovery of adsorbed Pb (II). Additionally, a machine learning algorithm, XGBoost tuned with Artificial Rabbits Optimization, was developed to predict the adsorption process, providing a robust tool for future use and improving the efficiency of Pb (II) removal.

Keywords Nanoparticles · Adsorption · Machine learning · Equilibrium · Kinetics · Thermodynamic

S. Madadgar · F. Doulati Ardejani
School of Mining Engineering, College of Engineering, University of Tehran, Tehran 1439957131, Iran

S. Madadgar · F. Doulati Ardejani
Mine Environment and Hydrogeology Research Laboratory (MEHR Lab), University of Tehran, Tehran 1439957131, Iran

Z. Boroumand
Nano-Bio Earth Laboratory, Applied Geological Research Center of Iran, Karaj, Iran

C. Butscher · R. Taherdangkoo (✉)
Institute of Geotechnics, TU Bergakademie Freiberg, 09599 Freiberg, Germany
e-mail: Reza.Taherdangkoo@ifgt.tu-freiberg.de

C. Butscher · R. Taherdangkoo
Freiberg Center for Water Research (ZeWaF), TU Bergakademie Freiberg, Akademiestr. 6, 09599 Freiberg, Germany

1 Introduction

The availability of safe drinking water is a crucial measure of progress in a community, which has recently become a serious concern worldwide. Population growth and the expansion of anthropogenic activities have increased the demand for water resources (Bora et al., 2014). However, the water quality is highly threatened due to the discharge of contaminants including metal ions, pharmaceuticals, oil spills, and organic dyes (Obiri-Nyarko et al., 2014). Based on the World Health Organization (WHO) reports, more than 40% of the world's population does not have access to safe and clean drinking water (Wang et al., 2020). The existence of heavy metals in water originated from industrial activities can be harmful to a wide range of organisms as they can negatively contribute to various diseases (Fu et al., 2014). The deposition of heavy metals like mercury, chromium, cadmium, arsenic, nickel, cobalt, lead, and copper can pose a serious ecological and public threat that requires immediate attention and efforts to mitigate their negative impacts. However, some metals are beneficial for human health in small quantities, according to the US Environmental Protection Agency (EPA), many of them are toxic and threatening, even in small dosages (Maret, 2016). Thus, immediate action is necessary to solve the global issue of heavy metal pollution and ensure the access to clean and safe potable water for all people around the world.

Lead is a hazardous heavy metal in aqueous media and causes significant water contamination challenges. It can accumulate in organisms through direct adsorption or entering the food chain and consequently cause harmful effects on the human body (Briffa et al., 2020). The maximum permissible lead concentration in drinking water is 0.05 mg/L, as mentioned by WHO, but even lower levels can hurt the internal body systems (World Health Organization, 2004, Ekramul Mahmud et al., 2016). Consequently, it is crucial to exclude lead from water to protect the environment and public health.

Various methods have been suggested for the removal of metals from water and wastewater, including chemical precipitation (Peng et al., 2020), membrane filtration (Peng et al., 2020), electrochemical techniques (Choumane & Peulon, 2022), ion exchange (Goyal et al., 2021), electrocoagulation (Titchou et al., 2021), reverse osmosis (Pezeshki et al., 2023), photocatalytic degradation (Ramalingam et al., 2022), and adsorption (Wang et al., 2021). However, these methods often have weaknesses such as high costs, partial removal of the contaminants, high energy consumption, and the production of toxic waste (Younas et al., 2021). Among these methods, adsorption is the most popular method due to its accessibility, sustainability, efficiency, biocompatibility, cost-effectiveness, easy implementation, and high ability to remove organic and inorganic contaminants from polluted water in an eco-friendly manner (Olya et al., 2013). The advantages of the adsorption process make it a preferred choice for solving the problem of heavy metal pollution in water resources.

The adsorption process utilizes several types of adsorbents, including biological sorbents (Xiang et al., 2022), industrial waste (Soliman et al., 2020), activated carbon (Mandal et al., 2021), synthetic polymers (Khodakarami et al., 2021), silica-based adsorbents (Taleb et al., 2024), and natural sorbents (Velarde et al., 2023). However, these adsorbents have some limitations such as low adsorption capacity and challenging separation, and their efficiency and capacity are influenced by factors like cost, performance, and reusability potential (Asadi et al., 2020a, b). Hence, the interest in nanostructured adsorbents is growing in order to address these limitations (Sadeghpour et al., 2023a, b). Nanomaterials have become popular as innovative adsorbents for the removal of organic and inorganic contaminants from water, as they have several distinct properties, such as high surface area, and significant adsorption capacity that make them effective in water purification applications (Asadi et al., 2020a, b). Various studies have confirmed the high efficiency of the different nanomaterials in the adsorption processes, as shown in Table 1.

Ferrite nanoparticles, such as spinel, Garnet, Hexaferrite, and orthoferrite, are remarkable in their crystalline structure. Particularly, spinel nanoparticles like $MnFe_2O_4$, have particularly gained attention for water and wastewater treatment. This is mostly because of their high surface area, higher adsorption capacity, biocompatibility, and significant magnetic characteristics in comparison to other ferrites (Marcelo et al., 2021). The utilization of $MnFe_2O_4$ nanoparticles has been extensive in the adsorption of pollutants, particularly heavy metals like lead in aqueous environments.

Table 1 Comparison of the adsorption capacities of various nanosorbents used for Pb(II) ions removal from aqueous solutions

Adsorbent	Adsorption Capacity (mg/g)	Ions	Refs
MNPs-Ca-alginate immobilized P. chrysosporium	176.33	Pb(II)	(Xu et al., 2012)
Fe_3O_4 MNPs	36.0	Pb(II)	(Yadava et al., 1991)
PEI-MNPs	83.33	Pb(II)	(Paul et al., 2006)
Magnetite Nanoparticles	53.1	Pb(II)	(Rajput et al., 2016)
Water-soluble Fe_3O_4 nanoparticles	96.8	Pb(II)	(Wang et al., 2012)
Fe_3O_4 cyclodextrin polymer nanocomposites	64.5	Pb(II)	(Badruddoza et al., 2013)
Magnetic nanoparticle clusters (grain 5)	177.5	Pb(II)	(Lin et al., 2013)
$MnFe_2O_4$ Nanoparticles	75.75	Pb(II)	(Hassan et al., 2021)
($MnFe_2O_4$) Magnetic wild plant biochar	129.87	Pb(II)	(Fuat & Cumali, 2021)
Bio-modified magnetic nanoparticles with Terminalia arjuna bark extract (TA@MNPs)	210.5	Pb(II)	(Das et al., 2022)
MDA-Fe_3O_4	333.3	Pb(II)	(Sharahi et al., 2017)
Quercetin-MNP	68	Pb(II)	(Jian et al., 2018)
Fe_3O_4@SiO_2-NH-MFL nanoparticles	150.3	Pb(II)	(Zhang et al., 2019a, b)

Non-toxic and non-metallic g-C_3N_4 nanosheets also have high adsorption capabilities and have been widely used for water treatment and heavy metals removal from contaminated water (Mortazavi et al., 2020; AbuMousa et al., 2022; Mulungulungu et al., 2021; Shen et al., 2015). However, there are challenges with their reusability and separation from the treated wastewater. To solve this problem, combining g-C_3N_4 with magnetic materials like $MnFe_2O_4$ as the magnetic support material can facilitate the separation by using external magnetic fields. The synergistic effects of these innovative nanomaterials make them a promising option for sustainable water purification processes (Xie et al., 2022; Koizumi et al., 2014).

Spinel ferrite nanoparticles can be synthesized using different methods, such as ultrasonication (Amulya et al., 2021), solvothermal (Li et al., 2015), hydrothermal (Zhang et al., 2019a, b), microemulsion (Baig et al., 2019), thermal decomposition (Singh & Chandra, 2018), co-precipitation (Eyvazi et al., 2020a, b), template-synthesis (Kogularasu et al., 2018), sol–gel (Wang et al., 2018), microwave-induced combustion (Sezgin et al., 2015), and other methods. In this study, the direct co-precipitation method was used to synthesize $MnFe_2O_4$ nanoparticles, which is a common method for it is cost-effective, and can produce in controlled size and composition (Hu et al., 2007).

Furthermore, phytoremediation, as a bioremediation approach, has gained significant attention for water remediation for its significant efficacy, high adsorption capacity, economic viability, and being eco-friendly (green) (Yaashikaa et al., 2022). Various studies have demonstrated the effective elimination of metal ions from aqueous solutions and wastewaters using biosorbents and plants. For instance, scientists successfully obtained Pb (II) ions removal efficiency of 94.47% using *Rapeseed biomass* (Morosanu et al., 2017). In other studies, *Henna* powder could extract 97.8% of lead from a solution with 93.5 mg/L lead in 49 min (Davarnejad et al., 2020), and *Sargassum tennerium* exhibited maximum lead adsorption capacity of 6.657 mg/g (Bai & Venkateswarlu, 2018). In addition, *Pinecone was* able to extract Pb (II) from industrial wastewater with maximum adsorption capacity of 27.53 mg/g (Momčilović et al., 2011), and dried *Lemna perpusilla* could eliminate above 95% of Pb (II) from a solution with 50 mg/L Pb (II) in 210 min (Tang et al., 2013).

Chrysopogon zizanioides (CZ) is a resilient perennial plant native to Asia, which has been known as a low-cost adsorbent for removing toxic metals from polluted water and soil for its availability, sustainability, easy use, and effectiveness, even in harsh conditions (Danh et al., 2009; Truong, 1999). CZ root powder has been previously

recognized as an effective super-adsorbent, with high ability to remove heavy metals from aqueous solutions, with maximum adsorption capacity of 31.78 mg/g for Pb in previous research (Madadgar et al., 2023).

The primary objective of this research was to develop a novel adsorbent by employing a natural hyperaccumulator plant, CZ, along with a nanosorbent, to examine its effectiveness in improving the removal efficiency of Pb (II) ions from contaminated water. Additionally, the research aims to develop a more cost-effective nanosorbent, as well as giving magnetic properties to the adsorbent that facilitates its separation, since producing nanosorbents can be quite expensive. For this purpose, the adsorption capacities of CZ/$MnFe_2O_4$/g-C_3N_4 was examined to ensure that the novel synthetized nanosorbent would be efficient, compared to different nanoparticles used in previous studies, while being cost-effective. Furthermore, the predictive modeling of Pb(II) adsorption efficiency was conducted using Extreme Gradient Boosting (XGBoost), a robust and scalable machine learning algorithm. To enhance the model's predictive performance, hyperparameter tuning was performed using the Artificial Rabbits Optimization (ARO) algorithm. The resulting machine learning model is a scalable and efficient tool for Pb(II) ions remediation in contaminated water.

2 Materials and Methods

2.1 Materials

The chemical reagents employed in this study were of analytical grade and did not require further purification, included root powder from Chrysopogon zizanioides (CZ) plant, ultra-pure graphite fine powder (CAS number: 7782–42–5), urea, ethanol, Nitric Acid (HNO_3), Sodium Hydroxide (NaOH), Manganese Sulfate Tetrahydrate ($MnSO_4 \cdot 4H_2O$) salt, Ferric Chloride Hexahydrate ($FeCl_3 \cdot 6H_2O$) salt, and Lead(II) Nitrate (Pb $(NO_3)_2$), all sourced from Merck company. All solutions used in the laboratory were of analytical grade and prepared using deionized (DI) water (18.2 MΩ.cm).

2.2 Synthesis of Root/MnFe2O4/g-C3N4 Nano Composite

To synthesize $MnFe_2O_4$ nanoparticles, a direct co-precipitation method was utilized (Ghobadi et al., 2018), involving the initial dissolution of a certain quantity of $MnSO_4 \cdot 4H_2O$ salt and $FeCl_3 \cdot 6H_2O$ salt in a 1:2 M ratio between Mn:Fe, followed by vigorous stirring in 100 ml of ultrapure deionized water at the controlled temperature of 80°C. Afterward, 8 M NaOH, preheated to 80°C, was added abruptly until the pH reached 11, and stirring was continued for an additional 30 min to ensure complete growth of nanoparticle crystals. For the preparation of graphite carbon nitride (g-C_3N_4), as described in previous research (Saeidpour et al., 2022), a Polycondensation method was employed. Initially, 10 g of urea was placed in a porcelain crucible with a lid and heated in a vacuum oven at 450°C for 2.5 h at a heating rate of 15°C per minute. The resulting light pale-yellow powder was grinded and stored for further use. Subsequently, 200 mg of g-C_3N_4 was dissolved in deionized water, added to the previous product, and stirred for an additional 45 min. Following this, 2 g of CZ root powder, obtained using a planetary ball mill, was introduced to the solution, and subjected to ultrasonication for 30 min. Stirring was then continued at 80°C for 30 min. Afterward, 8 M NaOH, preheated to 80°C, was added abruptly until the pH reached 11, and stirring was continued for an additional 30 min to ensure complete growth of nanoparticle crystals. Finally, the black magnetic precipitates were separated using a strong magnet, washed multiple times with Acetone and deionized water, respectively. The resulting nanoparticles were then dried at 60°C for 24 h (Sadeghpour et al., 2023a, b).

2.3 Characterization

The synthetized nanosorbent (CZMNCN) was analyzed through various analyses to determine its properties. Functional groups of the nanosorbent were characterized using an AVATAR (Thermo, Waltham, MA, United States) over a working range of 350–7800 cm−1. Scanning electron microscopy (SEM) was used to characterize the surface morphology, particle size, and chemical composition of the nanoparticles. This analysis was performed using the TESCAN MIRA III field emission scanning electron

microscope (FE-SEM) in combination with an energy dispersive spectrometer (EDS) for elemental analysis. The concentrations of Pb (II) elements were measured using an Agilent 7500 inductively coupled plasma mass spectrometry (ICP-MS). The surface area, pore size distribution, and pore volume of the nanosorbent were determined through Brunauer–Emmett–Teller (BET) analysis using a Microtrac-BELSORP-mini-instrument, which covers a range of 0.35–200 nm and a relative pressure (p/p0) of 0.990. The magnetic characteristics of the nanoparticles were assessed using a vibrating sample magnetometer (VSM) from Meghnatis Daghigh Kavir Co. (Iran) at ambient temperature (298 K). Raman spectroscopy was conducted to provide detailed information about chemical structure, polymorphy, crystallinity and molecular interactions with a Takram N1-541 (Iran) spectrometer (Nd: YAG laser). The zeta potential and the size of the nanoparticles were assessed utilizing a Horiba SZ-100z instrument by Dynamic Light Scattering (DLS) method, and the pH of the solutions was measured using a Metrohm 827 digital pH meter.

2.4 Adsorption Experiments

Response Surface Methodology (RSM) with Central Composite Design (CCD) were employed in order to optimize the experimental designs and minimize the number of required tests, using Design-Expert software (DX-7). RSM is a statistical method that facilitates the modeling and optimization of processes by identifying the effects of different variables and minimizing the number of required tests. CCD was utilized as an accurate method for optimization of the variables and responses, with RSM to develop the adsorption experiments (Adeleke et al., 2019). Five critical parameters were chosen for investigation: initial lead concentration, contact time, temperature, pH, and adsorbent dosage.

The adsorption of Pb (II) ions was conducted in a batch system. The effect of the adsorbent dosage was investigated by using dosages between 1.55–3 g/l to an Erlenmeyer containing 100 mL of contaminated solution and rotating in a FineTech-SKIR-601 shaking incubator at 250 rpm. As the optimal amount of adsorbent was found, the optimal amount was added to the contaminated solution in 100 mL Erlenmeyer flasks, which were then shaken at 250 rpm. Then, the adsorbent was separated from the solution using a strong Nd-Fe-B magnet (grade N42, magnetic field strength of 1280 mT). The quantity of metals absorbed by the adsorbent were investigated at different pH levels in a range from 1 to 6. The pH values were adjusted with a 0.15 M solution of NaOH and HNO3 solution. Kinetic studies were conducted to assess the effect of contact time on the adsorption process for 5–90 min, under constant conditions of 250 rpm agitation speed and 298 (K) temperature. The reaction kinetics were analyzed using various models, including the Pseudo-first-order, Pseudo-second-order, and Intra-particle diffusion models. Isotherm studies were conducted at different initial Pb (II) concentrations (10–100 mg/L) in 100 mL of the contaminated solution, at a constant temperature of 298 K. Furthermore, the distribution of the nanosorbent between the solid and liquid phases was evaluated using various isotherm models, including Langmuir, Freundlich, and Dubinin-Radushkevich. Thermodynamic studies were also conducted to examine the impact of temperature on the adsorption process at 298 K, 313 K, and 323 K. A 100 mL solution containing 1.55 g/L of the nano adsorbent and initial Pb (II) concentrations of 100 mg/L and 10 mg/L was stirred for 2 h in a temperature-controlled shaking incubator at 250 rpm. Thermodynamic studies were then carried out using the relevant equations. The adsorption capacity of the adsorbent at equilibrium and the Pb (II) removal percentage were determined using Eqs. (1) and (2), respectively (Liu et al., 2021):

$$q_e = \left(C_0 - C_e\right) \times \frac{V}{M} \tag{1}$$

$$R = \frac{(C_0 - C_e)}{C_0} \times 100 \tag{2}$$

where the (q_e) adsorption capacity (mg/g) can be calculated using the (C_0) initial concentration (mg/l) and the (C_e) final concentration of Pb (II) in the solution, and M (g) is the mass of the adsorbent, and V (L) represents the volume of the solution, and R (%) denotes the removal percentage of the adsorbate from the solution.

2.5 Desorption Studies

Desorption studies are crucial in assessing the reusability and metals recovery potential of the adsorbent particles in an acidic environment. After the

adsorption process, the separated nanoparticles were added into a 100 mL solution of 0.15 M nitric acid and stirred for 2 h at 250 rpm. To evaluate the stability and effectiveness of the nanosorbent after multiple washing cycles, the whole process was repeated for 3 cycles. Then, the resulting solutions were collected, and the nanoparticles were separated to determine the reusability of the nanoparticles and Pb (II) recovery. The investigations were conducted at ambient temperature. After each stage, the pH levels of the solutions were measured using a Metrohm pH Meter 744, and the Pb (II) concentrations were determined via UV–VIS spectroscopy (Agilent-8453).

2.6 Machine Learning Modeling

XGBoost (Extreme Gradient Boosting) is a highly efficient, scalable machine learning algorithm designed for regression, classification, and ranking tasks (Chen et al., 2016; Kooti et al., 2024a). It builds an ensemble of decision trees in a sequential manner, optimizing a custom loss function using gradient descent (Chen et al., 2016). In this implementation, the XGBRegressor is configured with five hyperparameters: n_estimators (number of trees), max_depth (tree depth), eta (learning rate), subsample (fraction of samples for each tree), and colsample_bytree (fraction of features used for each tree). These parameters are tuned to minimize the model's prediction error, measured by the Mean Squared Error (MSE).

To optimize these hyperparameters, the Artificial Rabbits Optimization (ARO) algorithm is applied. The ARO algorithm is a bio-inspired meta-heuristic technique based on the survival strategies of rabbits, including detour foraging and random hiding. Detour foraging represents the exploration phase, where rabbits forage far from their nests to minimize predator risks. Random hiding models the exploitation phase, where rabbits randomly select a burrow from multiple created near their nests for safety. The transition between these strategies is governed by an energy factor, which decreases with iterations, balancing exploration and exploitation as the algorithm progresses. Key parameters of ARO include the population size, representing the number of candidate solutions (rabbits) maintained during optimization; the number of iterations, defining the total computational steps to refine solutions; and the epoch count, which determines the number of optimization cycles for adaptive variants (Wang et al., 2022).

The evolutionary optimizer uses a population of candidate solutions and iterates over several generations (epoch = 50, pop_size = 30) to find the best configuration. The fitness function evaluates each candidate solution by training the XGBRegressor on the training set and computing its MSE on the test set. This process is repeated across 20 simulations to ensure robustness and reliability of the optimization. The best hyperparameter set and corresponding MSE are identified from the results and stored for further analysis. The two layer optimization (1) integration of ARO-based optimization with XGBoost and (2) the repetition of the process for 20 times enables effectively balancing exploration and exploitation to find optimal configurations for predictive performance (Kooti et al., 2024b; Taherdangkoo et al., 2024). The framework's scalability and adaptability make it suitable for relatively small datasets.

The input dataset consists of the initial concentration (ppm), adsorbent dosage (g/L), pH, temperature (°C), and time (minute), while the adsorption capacity (mg/g) is the output. The dataset was split into training and testing subsets, with 80% of the data allocated for training and 20% for testing. The split was performed using a random seed fixed to 90 to maintain reproducibility, ensuring consistency in the division of training and testing data across multiple runs.

3 Results and Discussion

3.1 Characterization of CZ/$MnFe_2O_4$/g-C_3N_4

FTIR analysis used to identify surface functional groups, bonding information, and chemical compounds of the synthetized nanosorbent, before and after the adsorption (Fig. 1). As can be seen in the FTIR spectrum of CZ/$MnFe_2O_4$/g-C_3N_4 nanoparticles, the peak at 580 cm^{-1} is attributed to the Mn–O and Fe–O vibrations within the spinel structure of the MnFe2O4 component, as well as the deformation vibrations of metal–oxygen-hydrogen (M–O-H) groups (Kefeni et al., 2017). The peak seen around 1050 cm^{-1} shows C-O stretching vibrations in polysaccharides, alcohols, ethers, or esters, or metal-O-C

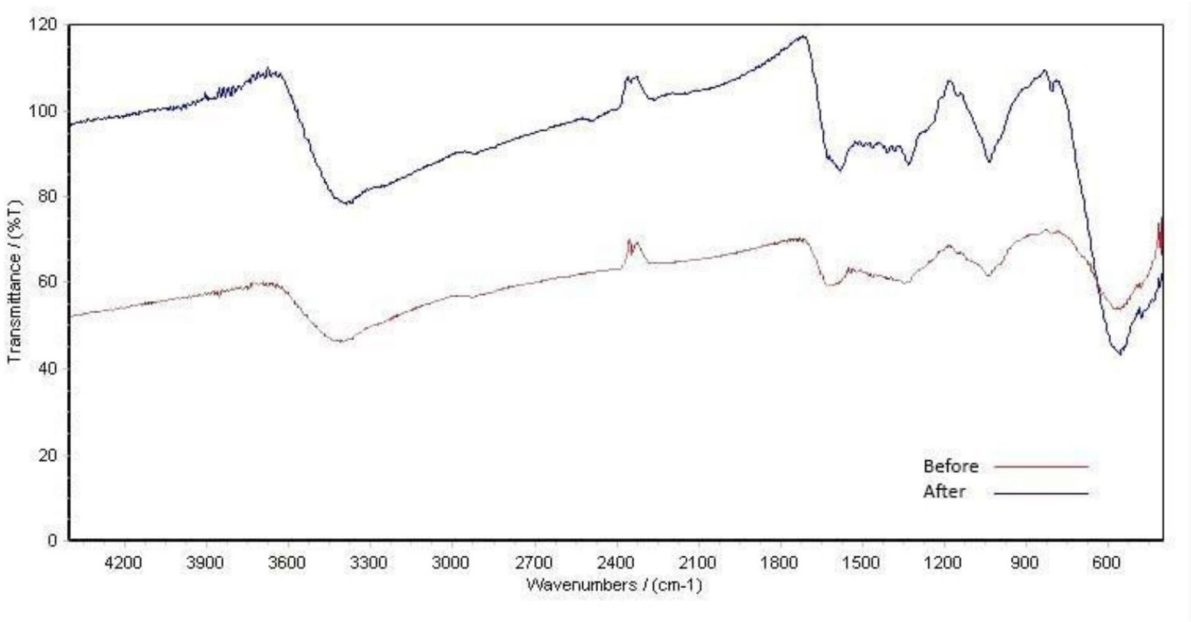


Fig. 1 FTIR spectra before and after Lead ions adsorption onto CZMNCN

vibrations, suggesting interaction between MnFe2O4 and organic carbon groups in the plant (Socrates, 2004; Ghobadi et al., 2018). The peak around 1300 cm^{-1} is attributed to the bending vibrations of C-O–H groups. This peak may also show the presence of metal-O–H vibrations and indicates involving of hydroxyl groups with the metal oxide in nanoparticles (Socrates, 2004). Peak around 1650 cm^{-1} can be attributed to the C = O stretching vibration, which can indicate the presence of carboxylate, carbonyl or Amide groups on the nanoparticle surface (Stuart et al., 2004). The inverted peak around 2300 cm^{-1} is likely related to CO_2 adsorption and indicates that CO_2 is adsorbed on the surface. The presence of this peak suggests that surface chemistry may affect the nanoparticles' capacity for Pb removal. A peak around 2900 cm^{-1} represents the C-H stretching vibrations, which can be attributed to the organic functional groups present on the nanoparticle surface (Gupta et al., 2011). The peak around 3350 cm^{-1} illustrates the presence of O–H stretching vibrations for hydroxyl groups (Mohan & Pittman, 2007).

Some changes are observed in peaks' sharpness, intensity, and position in the FTIR spectra after Pb adsorption. It can generally be for the availability of functional groups that are responsible for the removal of Pb ions. After adsorption, the intensity of some peaks increased, which shows increased interactions between Pb ions and the nanosorbent surface. The rise in peaks intensity, especially near 1650 cm^{-1} (C = O) and 1050 cm^{-1} (C-O), indicates that the concentration or presence of these functional groups has increased after Pb adsorption.. This may be attributed to the attachment of Pb ions to these groups, that can make them more visible on the $MnFe_2O_4$/g-C_3N_4 nanosorbent surface (Wang & Chen, 2009). Moreover, shifts in the positions of peaks or their sharpness can indicate some changes in functional groups or bondings. These changes approve the successful physisorption of Pb ions onto the CZ/$MnFe_2O_4$/g-C_3N_4 nanosorbent and determines its efficacy for water treatment.

Scanning electron microscopy coupled with energy dispersive X-ray detector (SEM–EDX) was employed to characterize the morphology, particle size, and elemental composition of the synthesized CZ/$MnFe_2O_4$/g-C_3N_4 before (Fig. 2a, c) and after adsorption (Fig. 2b, d). The SEM images revealed a highly porous, network-like and spherical-shaped CZ/$MnFe_2O_4$/g-C_3N_4 nanoparticles (average size of 53 nm) with a rough and irregular surface. It shows the large surface area and abundant adsorption sites of the nanosorbent that can facilitate the lead

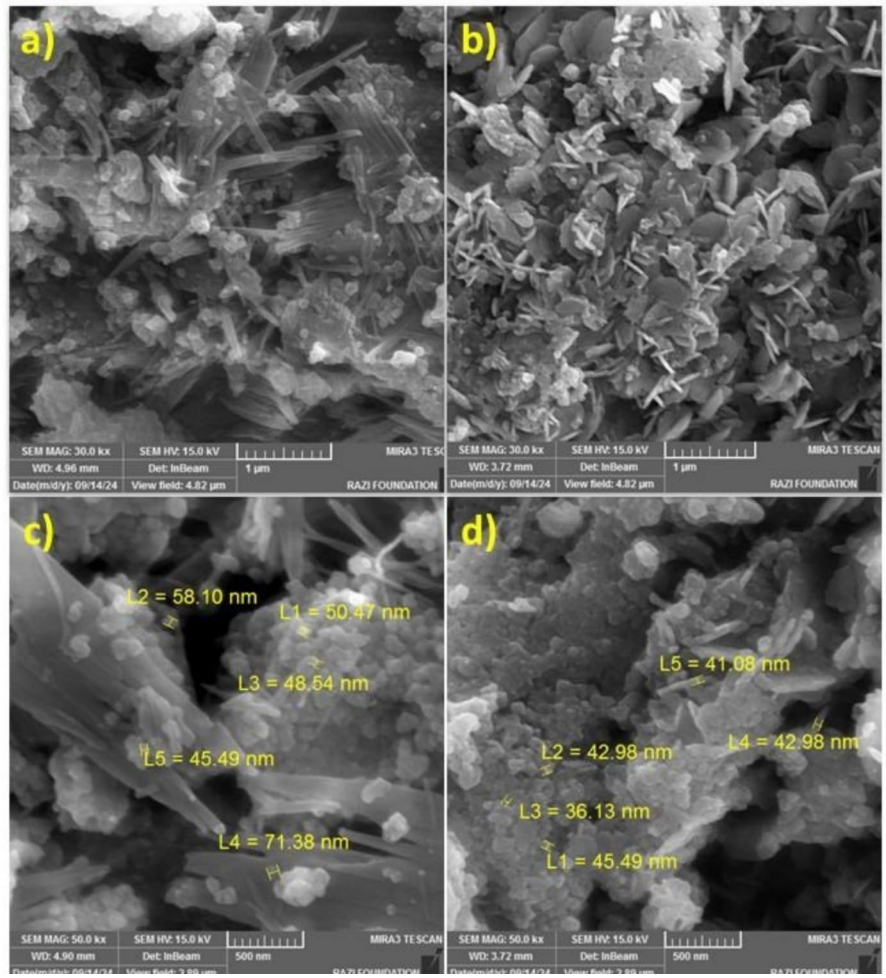


Fig. 2 SEM images of CZMNCN; (**a**, **c**) before Lead ions adsorption, (**b**, **d**) after Lead ions adsorption

removal. The images show spherical-shaped particles, that can be attributed to $MnFe_2O_4$ and the nanosheet that indicates g-C_3N_4, which proves the CZ surface is well-coated with nanoparticles. However, the porous structure was altered after Pb (II) adsorption, with the formation of agglomerated spherical particles. The elements were determined by EDX, before (Fig. 3a) and after (Fig. 3b) the adsorption. The EDX analysis confirmed the presence of Pb (II) in the CZ/$MnFe_2O_4$/g-C_3N_4 samples, which indicated the successful uptake of Pb (II) by the nanoparticles. The EDX results also show the presence of Mn, Fe, O, C, and N elements, which can illustrate the composition of the nanosorbent.

The particle size distribution of the nanoparticles was analyzed using dynamic light scattering (DLS) measurements. The DLS results indicate that the dispersion of the CZ/$MnFe_2O_4$/g-C_3N_4 nanoparticles

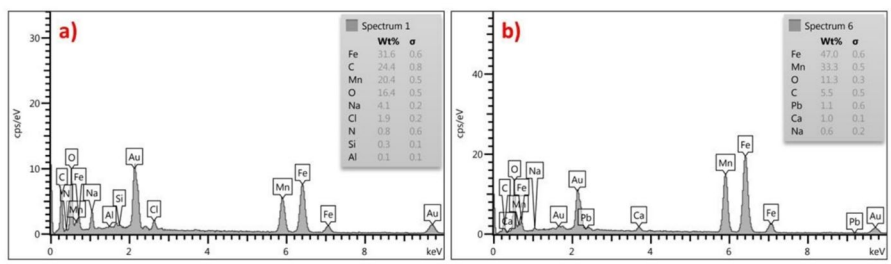


Fig. 3 EDS analysis of CZMNCN; before (**a**) and after (**b**) Lead ions adsorption

was homogeneous, with an average particle size of 256.9 nm that is observed in the major peak. However, scanning electron microscopy (SEM) images revealed that the CZ/$MnFe_2O_4$/g-C_3N_4 particles had an approximate size range of 36–71 nm, with an average size of around 53 nm. The discrepancy between the DLS and SEM measurements can be attributed to the different principles of the two techniques. DLS measures the hydrodynamic diameter of particles in solution, which includes the solvation layers formed around hydrophilic particles. This can cause an overestimation of the nanoparticle size compared to the actual dry particle size as measured by SEM, which represents the particles in the dried form.

Zeta potential is an important parameter in the characterization of nanoparticles in suspension and is closely related to surface morphology of the nanoparticles. Zeta potential analysis indirectly indicates the stability of nanoparticles in a dispersed solution. Nanoparticles are generally considered stable when the zeta potential value is less than −30 mV or greater than 30 mV. The zeta potential value observed for the CZMNCN was −28.1 mV, as shown in Fig. 4. This indicated high stability for the CZ/$MnFe_2O_4$/g-C_3N_4 nanoparticles. In addition, the negative charge on the particle surface favored the adsorption of Pb (II) ions with positive charge.

The synthesized nanocomposites were also characterized by Raman spectroscopy to study the composition and properties of the CZ/$MnFe_2O_4$/g-C_3N_4 nanosorbent (Fig. 5). Raman spectroscopy is a crucial technique for studying the characteristics of carbonaceous materials, particularly g-C_3N_4, within nanocomposite structures (Rathi et al., 2020). The Raman spectrum of the nanosorbent showed two distinct peaks. The peak at 102 cm^{-1} can be attributed to the vibrations of the metal–oxygen (M–O) bonds, specifically the $MnFe_2O_4$ spinel phase in the nanocomposite, which confirms the presence of the magnetic nanoparticles. The peak at 1583 cm-1 corresponds to the

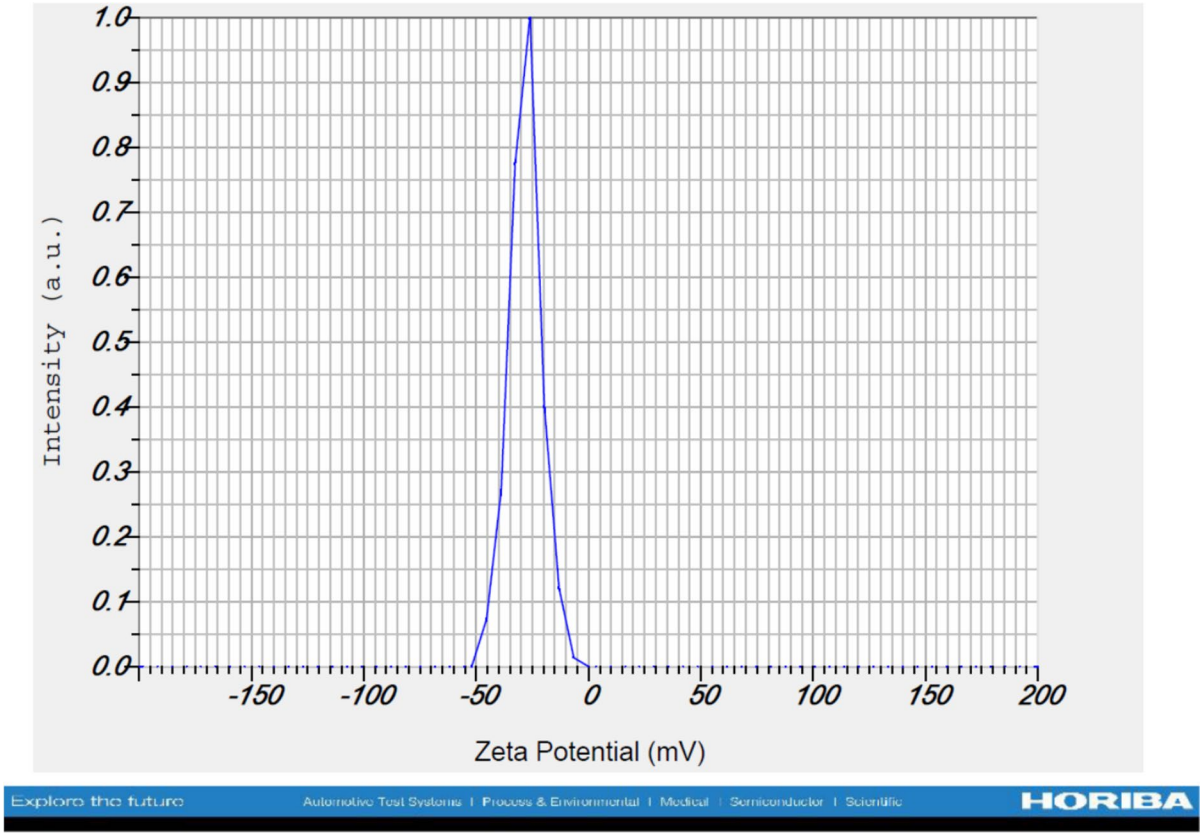


Fig. 4 Zeta Potentials of CZMNCN

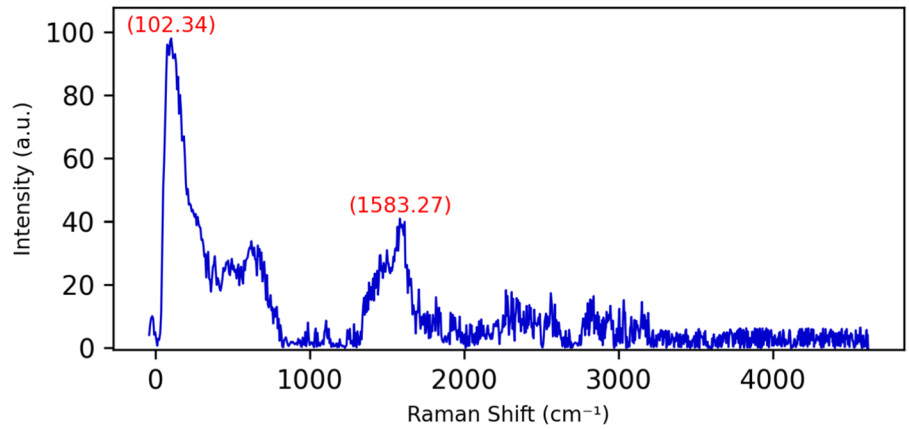


Fig. 5 Raman spectra of CZMNCN

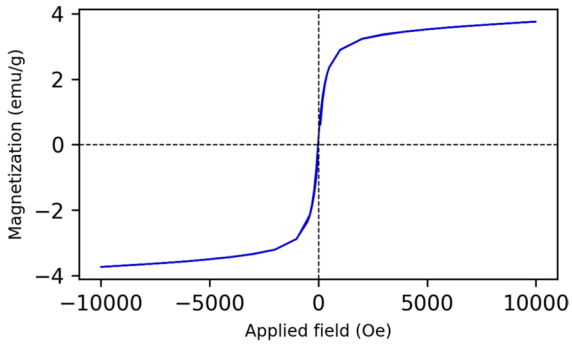


Fig. 6 Magnetic hysteresis loop of CZMNCN

G-band, which is associated with the in-plane stretching vibrations of the sp2-hybridized carbon atoms in the graphitic carbon nitride structure. The presence of these two characteristic Raman peaks approves the successful incorporation of both $MnFe_2O_4$ nanoparticles and g-C_3N_4 sheets within the nanosorbent. G is the main peak in graphite structures, where G shows the regular bond structure of sp2 (Wang et al., 2017). This synergistic combination of the magnetic and photocatalytic components is likely to improve the adsorption and lead removal capabilities of the nanocomposite.

Magnetic characterization of the synthesized nanosorbent was conducted using a vibrating sample magnetometer (VSM) at room temperature. As shown in Fig. 6, the CZ/$MnFe_2O_4$/g-C_3N_4 nanohybrids exhibited a saturation magnetization of 3.82 emu/g, which indicates superparamagnetic properties with near-zero coercivity and remanence, as can be seen by the S-shaped hysteresis loop under a 10 KOe magnetic field (Xu et al., 2013). These magnetic properties allow the nanoparticles to disperse in an aqueous environment without an external magnetic field. Furthermore, the non-magnetic nature of CZ and g-C_3N_4 components did not negatively affect the overall magnetization, which was sufficient for the necessary magnetic behavior. The nanosorbent's strong magnetic properties facilitate its recovery from an aqueous solution by an external magnetic field after the adsorption process.

Table 2 The results of BET analysis

Adsorbents	BET surface area (m^2/g)	Total pore volume (cm^3/g)	Average pore diameter (nm)
CZMNCN	40.73	2.04	0.643

The surface area, porosity, and pore size characteristics of the CZ/$MnFe_2O_4$/g-C_3N_4 nanosorbent were determined by BET analysis. The results showed a BET surface area of 40.73 m^2/g, pore volume of 2.4 cm^3/g, and average pore diameter of 0.643 nm (Table 2), which indicates a mesoporous structure (2–50 nm) that can facilitate the adsorption of Pb (II) ions. The porous nature of the nanosorbent is beneficial for effective adsorption of heavy metals. Furthermore, the high surface area of the CZ/$MnFe_2O_4$/g-C_3N_4 nanocomposite improves its adsorption capacity for lead removal (Abdel-Wahed et al., 2020).

3.2 Experimental Studies

3.2.1 Effect of pH on Adsorption

Studying the effect of pH on the adsorption is crucial for optimizing environmental remediation processes, since pH of the solution can have a significant

impact on the adsorption process. The pH can contribute to the adsorbent surface charge, the ionization potential and distribution of metal ions. Studies on Pb (II) adsorption have shown that pH can modify the surface charges of both the absorbent and Pb (II) ions and affect the electrical charge of the adsorbent (Ugwu et al., 2020; Eyvazi et al., 2020a, b). Figure 7 depicts the relationship between Pb (II) recovery and pH values. The results indicate that adsorption capacity is directly related to pH. At more acidic pH levels, adsorption is lower due to abundance of hydrogen ions (H^+) that compete with Pb (II) cations for available adsorption sites on the nanoparticles surface. However, with the increase of pH and decrease of H^+ concentration, the active surface sites become less occluded and higher adsorption of Pb (II) ions occurs (Niu et al., 2019). Maximum Pb adsorption by the nanoparticles was observed at pH 5. At more acidic pH levels below 5, the electrostatic attractive forces were gradually diminished, which resulted in lower removal efficiency. Above pH = 5, Pb began to react with hydroxide ions (OH^-) and form hydroxide precipitates, which caused the adsorption to considerably decline (Greenwood & Earnshaw, 2012). The nanoparticles exhibited approximately 99% Pb adsorption in the pH range of 4 to 6. Consequently, pH 5 was determined to be optimal for Pb adsorption on the nanoparticles and further experiments. Furthermore, the Eh–pH diagram was used to determine the charges of the Pb ions and the stable species, which showed that in an acidic environment and before Ph = 6 and Eh = 0.2, the dominant ions are Pb^{2+} (Takeno, 2005). Moreover, the point of zero charge (PZC) of the nanosorbent was studied and illustrated in Fig. 8. As observed, the nanosorbent surface charge was negative in pH above 4, which confirms the high adsorption rate of Pb ions in this range of pH.

3.2.2 *Effect of Adsorbent Dosage on the Adsorption*

The adsorption capacity is highly affected by the adsorbent dosage that is used in the process. Generally, higher dosages can increase removal efficiency, however, excessive dosage can have a negative effect on the adsorption since it can lead to particle agglomeration and reducing the available active sites. Therefore, finding the optimal adsorbent amount is crucial, for it affects the efficiency, cost-effectiveness, and the economic feasibility of the water treatment process. Figure 9 shows the effect of adsorbent dosage on adsorption capacity and Pb (II) recovery. The results illustrated that as the nanosorbent concentration increased from 0.1 to 3 g/L, the Pb (II) recovery rose from 84.4% to 99.5%. As can be observed, with the increase in the adsorbent dosage up to 1.55 g/L, the adsorption rate increased significantly, although, further increases in the adsorbent dosages (1.55 g/L to 3 g/L) had minimal impact on the Pb (II) recovery. Consequently, the optimum adsorbent dosage was determined to be 1.55 g/L for further experiments, which results in higher removal efficiency (99.75%), as well as being economically efficient.

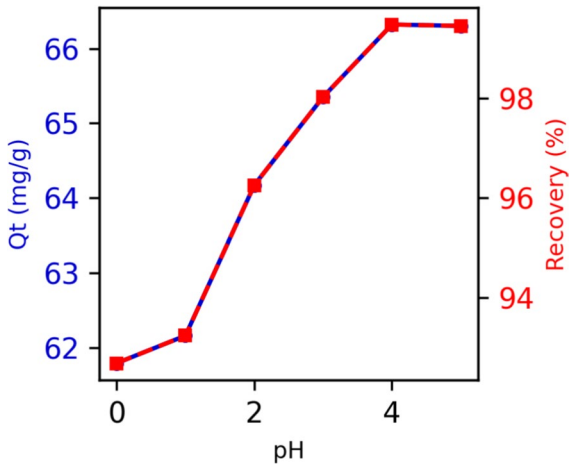


Fig. 7 Effect of pH on the Lead adsorption

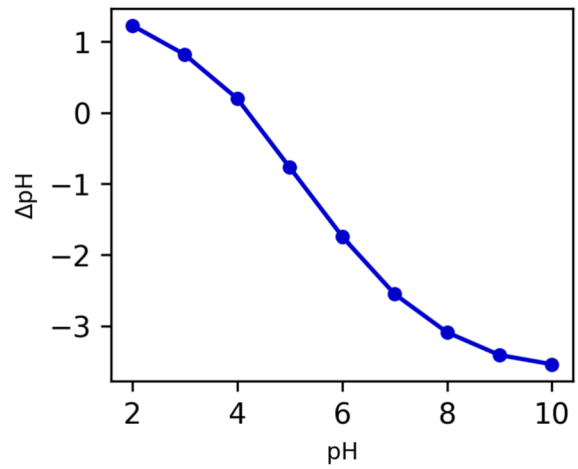


Fig. 8 Point of Zero Charge of CZMNCN

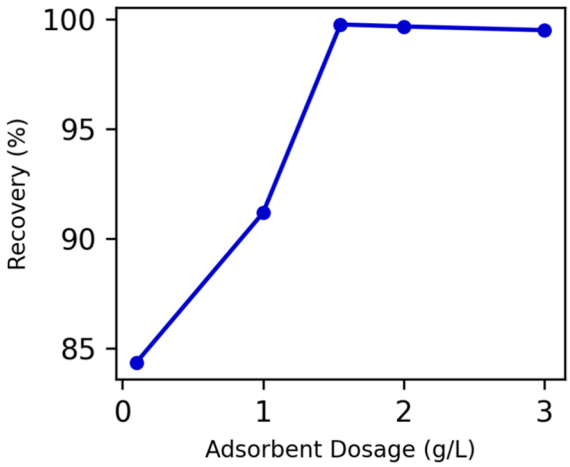


Fig. 9 Effect of the adsorbent dosage on the adsorption of Lead

3.2.3 Adsorption Kinetics and Effect of Contact Time

Studies on adsorption kinetics were conducted to investigate the effect of contact time of the adsorbent and Pb (II) ions, identify the optimal operational time for adsorption, as well as to develop a model for predicting the quantity of absorbed ions during treatment. For this purpose, various kinetics models including pseudo-first-order, pseudo-second-order, and intra-particle diffusion models were applied to analyze the experimental data, using Eqs. (3), (4) and (5), respectively (Bakhtiari & Azizian, 2015; Thue et al., 2018):

$$ln\left(q_e - q_t\right) = lnq_e - k_1 t \tag{3}$$

$$\frac{t}{q_t} = \frac{1}{K_2 q_e^2} + \frac{t}{q_e} \tag{4}$$

$$q_t = C + K_i\sqrt{t} \tag{5}$$

where, $K_1\left(min^{-1}\right)$ indicates the first-order kinetic constant, $K_2\left(g \cdot mg^{-1} \cdot min^{-1}\right)$ is pseudo-second-order rate constant, and $K_i\left(mg \cdot g^{-1} \cdot min^{-0.5}\right)$ refers to the intra-particle diffusion model constant. C is the adsorption constant and refers to the thickness of the boundary layer, z, and $q_e\left(\frac{mg}{g}\right)$ and $q_t\left(\frac{mg}{g}\right)$ represent the amount of contaminant adsorbed by the adsorbent at the time of equilibrium and the time "t (min)", respectively.

Based on the results presented in Table 3 and the correlation coefficients (R^2) values, it is obvious that the pseudo-second-order model exhibited a correlation coefficient value of 97.32%, which makes it the best fitting model with the experimental data, in spite of the pseudo-first-order and intra-particle diffusion kinetic models. Consequently, it can be concluded that the pseudo-second-order kinetic model described the adsorption mechanism of Pb (II) ions most appropriately. This model implies that the rate of occupation of adsorption sites is directly proportional to the second power of the number of vacant sites (Ali et al., 2016).

Figure 10 illustrates the investigation of the impact of adsorbent-adsorbate contact time on the removal of Pb (II) in 90 min duration, with an initial concentration of 100 mg/L. The results shown in Fig. 10 indicate that adsorption occurred rapidly, and it achieved a high adsorption rate within the first 5 min of exposure to the nanosorbent. However, when the time increased from 5 to 90 min, slight changes occurred in adsorption capacity. It implies that a remarkably high rate of adsorption can be achieved in a brief time duration, which shows the high ability of the CZ/$MnFe_2O_4$/g-C_3N_4 nanoparticles in Pb (II) removal. While 5 min was sufficient for adsorption, additional experiments were conducted for up to 90 min to obtain complete equilibrium and investigate further adsorption tests.

Table 3 Adsorption Kinetics models for Lead (initial concentration of 100 mg/L)

Contaminant	1 st order Plot: $ln\left(q_e - q_t\right)$ vs. t $q_e = exp(intercept)$ $k_1 = -slope$			2nd order Plot: $\frac{t}{q_t}$ vs. t $q_e = \frac{1}{slope}$ $k_2 = \frac{slope^2}{intercept}$			Intra-particle diffusion Plot: q_t vs. $t^{0.5}$ $K_i = slope$ $C = intercept$		
	R^2	$q_e\left(\frac{mg}{g}\right)$	$K_1\left(\frac{1}{min}\right)$	R^2	$q_e\left(\frac{mg}{g}\right)$	$K_2\left(\frac{g}{mg.min}\right)$	R^2	C	$K_i\left(\frac{mg}{g.min^{0.5}}\right)$
Pb (II)	0.93	2.87	0.011	0.97	12.16	0.003	0.94	24.18	3.927

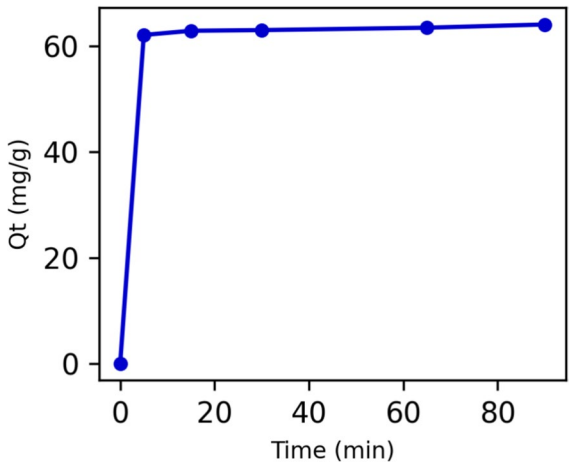


Fig. 10 Effect of contact time on the adsorption of Lead

3.2.4 *Adsorption Isotherms and the Effect of Initial Concentration*

Adsorption isotherms offer valuable information about the interactions between adsorbents and adsorbates when equilibrium is reached. Applying isotherms models such as Langmuir, Freundlich, and Dubinin-Radushkevich to the experimental data helps us comprehend the adsorption process. These models indicate the connection between the concentrations of adsorbates in both solid (q_e) and liquid phases (c_e) at constant temperature and pH (Netpradit et al., 2003; Doulati Ardejani et al., 2008).

Langmuir: The Langmuir isotherm model assumes monolayer adsorption occurs on specific homogeneous sites of an adsorbent surface, with each site possessing equal adsorption energy (Al-Rashdi et al., 2012). The non-linear and linear forms of Langmuir equation, which was applied to the experimental data is expressed by Eqs. (6) and (7), respectively (Langmuir, 1916):

$$q_e = \frac{q_m K_L C_e}{1 + K_L C_e} \text{ n} \tag{6}$$

$$\frac{c_e}{q_e} = \frac{1}{K_L q_m} + \frac{1}{q_m} c_e \text{ n} \tag{7}$$

where, C_0 and C_e (mg/L) represent the initial and equilibrium concentrations of the pollutant, q_e(mg/g) denotes the adsorption capacity at the equilibrium, q_m (mg/g) shows the maximum adsorption capacity of the adsorbent at the equilibrium, $K_L\left(\frac{L}{mg}\right)$ is the Langmuir isotherm constant, and K_L and q_m are obtained from the linear fit of C_e/q_e versus C_e.

Freundlich: The Freundlich isotherm model is commonly employed for comprehending the adsorption of metal ions, and assumes multilayer adsorption occurs on a heterogeneous surface, and it can also indicate the exponential distribution of active sites and their energy (Ayawei et al., 2015). The non-linear and linear forms of the Freundlich isotherm model are expressed by Eqs. (8) and (9), respectively (Freundlich, 1907):

$$q_e = K_F C_e^{\frac{1}{n}} \tag{8}$$

$$lnq_e = lnK_F + \left(\frac{1}{n}\right) lnC_e \tag{9}$$

where, $C_e\left(\frac{mg}{L}\right)$ denotes the equilibrium concentration, $q_e\left(\frac{mg}{g}\right)$ signifies the adsorption capacity at the equilibrium, K_F is referred to the Freundlich constant, and n indicates the intensity of adsorption. The Freundlich constants, K_F and n, can be obtained from the linear regression of lnq_e versus lnC_e. Moreover, n in Eq. (8) characterizes the type of isotherm in the Freundlich model, where the range of n between 1 and 10 indicates the appropriateness of the adsorption process. A value closer to 1 suggests that the heterogeneity of the surface is less significant, while a value closer to 10 signifies an increased level of homogeneity and a dominance of chemical adsorption over physical adsorption (Al-Rashdi et al., 2012).

The Dubinin-Radushkevich (D-R) isotherm model is an empirical tool that is commonly employed for analyzing the adsorption behavior, and it characterizes the heterogeneous surface by assigning Gaussian energy distribution and evaluating the energy associated with each adsorbed molecule (E). The non-linear and linear form of D-R adsorption isotherm model can be expressed as Eqs. (10) and (11), respectively (Dubinin, 1947):

$$q_e = q_m expexp\left(-\beta\varepsilon^2\right) \tag{10}$$

$$lnq_e = lnq_m - \beta\varepsilon^2 \tag{11}$$

where, $q_m\left(\frac{mg}{g}\right)$ represents the D-R monolayer capacity, ε shows the Polanyi adsorption potential related to the equilibrium concentration and expressed in

Table 4 Fitting Parameters of the Isotherm models for the adsorption of Lead by CZMNCN

Contaminant	Langmuir Plot: $\frac{C_e}{q_e}$ vs.C_e $q_m = \frac{1}{slope}$ $k_L = \frac{slope}{intercept}$			Freundlich Plot: lnq_e vs.lnC_e $n = \frac{1}{slope}$ $k_F = exp(intercept)$			Dubinin-Radushkevich Plot: lnq_e vs.ϵ^2 $q_m = exp(intercept)$ $E = \frac{1}{(2(-slope))^{0.5}}$		
	q_m $\left(\frac{mg}{g}\right)$	k_L $\left(\frac{l}{mg}\right)$	R^2	n	K_F	R^2	q_m $\left(\frac{mg}{g}\right)$	E $\left(\frac{KJ}{mol}\right)$	R^2
Pb (II)	217.39	0.011	0.90	1.06	235.09	0.95	252.2	2.42	0.95

Eq. (12), and β(mol2/J^2) is a constant associated with adsorption energy, and reflects the mean free energy E (kJ/mol) as Eq. (13):

$$\varepsilon = RTln\left(1 + \frac{1}{C_e}\right) \tag{12}$$

$$E = \frac{1}{\sqrt{2\beta}} \tag{13}$$

The free energy of the molecule (E) provides valuable insights into the adsorption process. When the adsorption energy is below 8 kJ, it signifies that the adsorption has taken place physically. On the other hand, if the adsorption energy falls within the range of 8 to 16 kJ/mol, it suggests that the adsorption process was chemical (Ouma et al., 2018).

Langmuir, Freundlich, and Dubinin-Radushkevich (D-R) isotherm models were employed in order to comprehend the adsorption mechanism. By plotting graphs of these models and evaluating their correlation coefficients, the most suitable isotherm was determined. Table 4 presents the results of isotherm models. The correlation coefficient values (R^2) indicate that the isotherm results of Pb (II) ions adsorption by the nanosorbent are most compatible with the Freundlich and Dubinin-Radushkevich models. This suggests that the adsorption of Pb (II) ions by the nanosorbent occurs on heterogeneous surfaces and is likely a multilayer process (Wang & Guo, 2020). Furthermore, the values of n in the Freundlich isotherm model suggest that adsorption process has been more physical rather than chemical. As well, the values of E in the D-R model, which are less than 8 kJ/mol, indicate physical adsorption. Moreover, according to Table 4, the maximum adsorption capacity of CZ/$MnFe_2O_4$/g-C_3N_4 for lead removal that obtained from the D-R model was 252.2 (mg/g), which indicates CZMNCN shows a significant adsorption capacity, as a novel nanosorbent. Figure 11 presents the adsorption isotherm data for Pb (II) adsorption by the nanosorbent, and it clearly illustrates that the adsorption capacity rises with the increase in initial Pb (II) concentrations.

3.2.5 *Adsorption Thermodynamics and Effect of Temperature*

Temperature is an important factor in understanding the adsorption mechanism, since it affects the thermodynamics of the process, and the adsorbent-adsorbate interactions (Sahmoune, 2019). Generally, the kinetic energy and mobility of adsorbate molecules and their diffusion increase in higher temperatures and consequently, it leads to faster adsorption (Alkherraz et al., 2020). Thus, by studying the temperature, the adsorption processes can be optimized in a more efficient way. Thermodynamic parameters like Gibbs free energy,

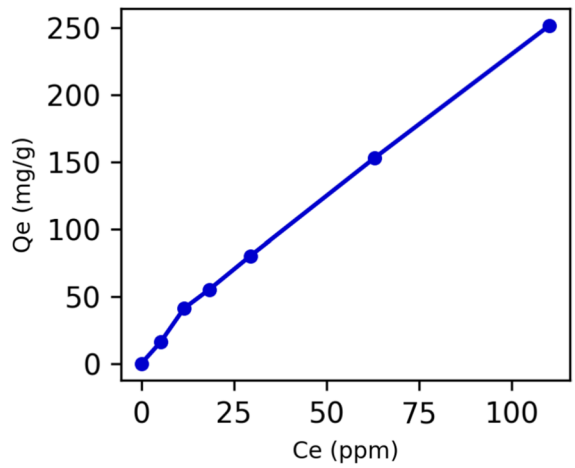


Fig. 11 Effect of initial concentration of Lead on the adsorption

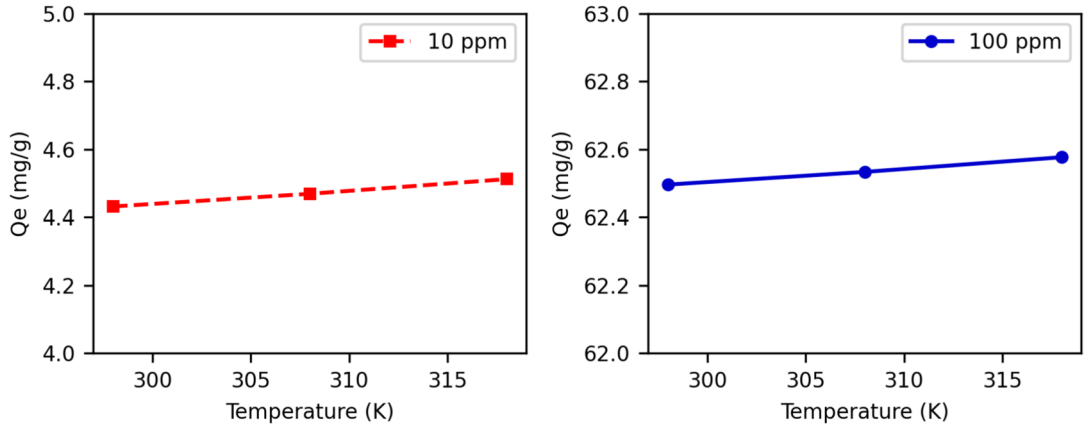


Fig. 12 Effect of temperature on the adsorption of Lead; (**a**) initial Lead concentration: 10 ppm, (**b**) initial Lead concentration: 100 ppm

standard entropy, and enthalpy must be calculated to understand the feasibility, direction, and nature of the adsorption process, in terms of being endothermic or exothermic (Greluk et al., 2010). The thermodynamic parameters were calculated using the Gibbs free energy change ($\Delta G°$) and Van't Hoff equation, represented by Eqs. (10) and (11) respectively (Wang et al., 2012):

$$\Delta G° = -RTlnK_L \tag{14}$$

$$lnK_L = \frac{-\Delta H^0}{RT} + \frac{\Delta S^0}{R} \tag{15}$$

where, $\Delta G°\left(\frac{KJ}{mol}\right)$ refers to the Gibbs free energy changes, R (8.314 J/mol/K) is the ideal gas constant, $K_L\left(\frac{l}{mol}\right)$ stands for the Langmuir constant, T (K) represents the absolute temperature, $\Delta S°$(KJ/K.mol) denotes the entropy changes, and $\Delta H°\left(\frac{KJ}{mol}\right)$ shows the enthalpy changes.

Figure 12 illustrates the impact of temperature on the adsorption capacity of Pb (II) using the nanosorbent, in the concentrations of 100 (mg/L) (a) and 10 (mg/L) (b) of Pb (II) ions, respectively. The results show that rising temperature leads to the slight increase in the adsorption capacity of Pb (II), which indicates that the adsorption process has an endothermic nature. Thermodynamic parameters related to Pb (II) adsorption on the nanosorbent are presented in Table 5. The positive values of $\Delta H°$ confirm that the adsorption reaction of Pb (II) by the nanosorbent is endothermic, and the negative values of $\Delta G°$ indicate that the adsorption reaction is possible and spontaneous (Massoudinejad et al., 2018). Moreover, the obtained $\Delta G°$ values in the range between 0 to −20 kJ. mol-1 suggest that the Pb (II) adsorption process follows a physisorption mechanism (Nodeh et al., 2016). Moreover, the results show positive values of the ΔS^0, which indicate the increased entropy at the boundary between the solution and nanoparticles (Asadi et al., 2020a, b). This increase in entropy indicates that the Pb (II) ions have become more dispersed from the bulk solution onto the available adsorption sites on the nanoparticle surface. This results in a more disorganized arrangement at the solid–liquid interface compared to the initial state. Furthermore, the $\Delta G°$ values declined as the temperature increased from 298 to 323 K, which indicates that higher temperatures are more advantageous for the adsorption process. This can be attributed to the fact that

Table 5 The adsorption thermodynamics parameters

Contaminant	$C_0(ppm)$	$\Delta G^0\left(\frac{KJ}{mol}\right)$			$\Delta S^0\left(\frac{Kj}{K.mol}\right)$	$\Delta H^0\left(\frac{KJ}{mol}\right)$
		298 K	313 K	323 K		
Pb (II)	100	−7.25	−7.69	−7.99	0.029	1.617
	10	−0.83	−0.99	−1.09	0.010	2.261

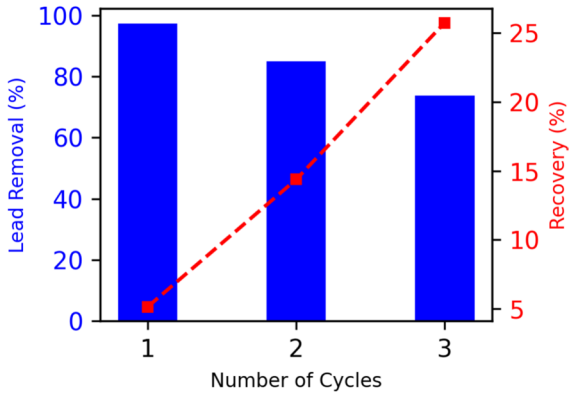


Fig. 13 The desorption of Lead and reusability and of CZM-NCN in 3 cycles

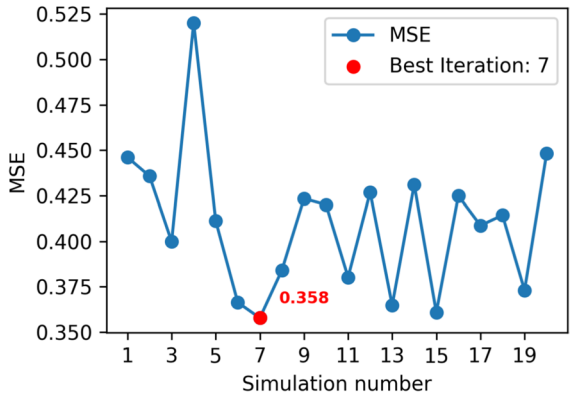


Fig. 14 The MSE value obtained on testing phase of 20 models. Best model identified as simulation 7 with an MSE of 0.358

the kinetic energy and mobility of adsorbate molecules and their diffusion increase in higher temperatures, and it leads to higher adsorption of Pb (II) ions on the nanosorbent surface (Alkherraz et al., 2020).

3.3 Desorption Study

In wastewater treatment, the adsorption–desorption and reusability studies of the spent adsorbents is considered as sustainable development strategy. These studies are important for evaluating the economic viability of the adsorption process using this specific nanosorbent, and can provide information about the potential environmental impacts of adsorbed heavy metals onto the nanoparticles. Hence, desorption studies were conducted for investigating the nanosorbent ability to be reused in multiple successive cycles of Pb (II) ion adsorption and desorption and also assessing the maintenance of its adsorption efficiency (Bayuo et al., 2024). For this purpose, after each adsorption cycle, the nanoparticles were separated by the magnet and introduced into a 100 mL solution which contained 0.15 M Nitric acid. Then, the nanoparticles were stirred for 2 h at 250 rpm before being removed from the magnet. As shown in Fig. 13, the adsorption rate decreased after each reuse cycle but remained economically viable for the removal of lead (II) ions. However, after 3 cycles, the adsorption capacity dropped to 73%, which meant that it was not attractive enough to continue further using the material for adsorption purpose. This is because, after 3 cycles, it would be necessary to either do a more thorough washing or increase the acid concentration for the adsorption to remain sufficiently effective. Although, this process can lead to losing some amounts of the nanosorbent in the process of washing with acid. Alternatively, some other materials such as graphene oxide can be added onto the nanosorbent by using different methods. Furthermore, as shown in Fig. 13, the recovery of Pb (II) ions from the nanosorbent increased after each cycle, which certifies the Lead removal. These results suggest that this nanosorbent can be effectively used for up to 3 successive adsorption–desorption cycles without significantly diminishing its adsorption efficiency.

3.4 Machine Learning Modeling

The machine learning modeling employed a two-layer optimization process to enhance the accuracy of Pb(II) adsorption predictions. The Artificial Rabbits Optimization and the subsequent evaluation was repeated 20 times, and the model having the lowest MSE on the test set was selected as the best-performing configuration. Figure 14 summarizes the MSE values for all 20 simulations, with the best model identified in simulation 7, achieving an MSE of 0.358

Table 6 Range and optimized values of hyperparameters

Hyperparameter	Lower bound	Upper bound	Range
Number of estimators	50	600	414
Maximum depth	1	20	7
Learning rate	0.01	0.9	0.1865
Subsample	0.1	0.9	0.6645
Colsample bytree	0.1	0.9	0.7844

on the test set. The optimized hyperparameter values for the best-performing model are listed in Table 6.

The model demonstrated high predictive accuracy, achieving an MSE of 0.069, RMSE of 0.264, and R^2 of 0.99 during the training phase. For the test phase, the model had an MSE of 0.358, RMSE of 0.598, and R^2 of 0.95, confirming its ability to generalize effectively. The regression plot in Fig. 15 reveals a strong agreement between experimental and predicted concentration values, indicating the model's reliability in capturing the underlying adsorption dynamics.

Residual analysis, as depicted in Fig. 16, further supports the model's robustness. The residuals for both training and testing phases are evenly distributed around zero, indicating unbiased predictions within the studied dataset. This supports the effectiveness of the machine learning framework in modeling the complex adsorption process.

By incorporating ARO for hyperparameter tuning and evaluating multiple independent runs, this study successfully developed a predictive tool for optimizing Pb(II) adsorption under the given experimental conditions. While the model achieved high accuracy and reduced reliance on extensive experimental work, its generalization remains limited by the dataset size and lack of external validation. Therefore, future studies with larger and more diverse datasets are required to establish broader applicability. Nonetheless, the integration of machine learning with systematic optimization shows its potential in advancing adsorption studies and water treatment technologies.

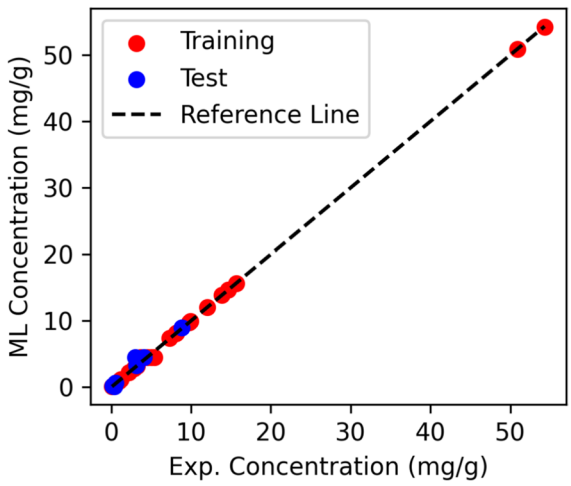


Fig. 15 Regression plot comparing the machine learning predictions and experimental data

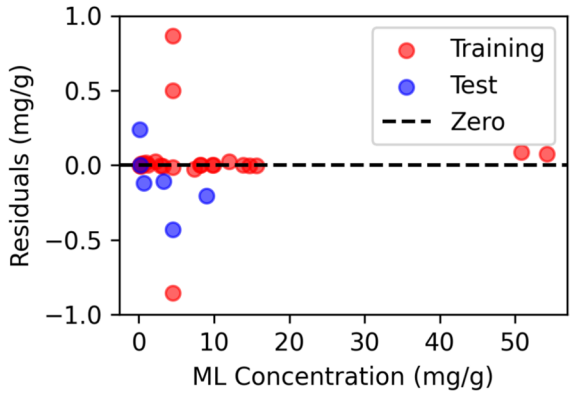


Fig. 16 Residual analysis of the residuals on both training and test phases

4 Summary and Conclusion

CZ root powder has previously been recognized as an effective super-adsorbent, with a significant ability to remove heavy metals from aqueous solutions, like 31.78 mg/g for Pb in previous research. This study aims to improve the efficacy of CZ root powder by integrating it with CZ/$MnFe_2O_4$/g-C_3N_4, a nanocomposite material with strong magnetic properties, to obtain facilitated separation as well as enhancing cost efficiency of the synthesis of nanosorbents. The results revealed that the novel CZ/$MnFe_2O_4$/g-C_3N_4 nanosorbent significantly improved the adsorption performance compared to the individual components. The maximum adsorption capacity of CZ/MnFe2O4/g-C3N4 for Pb adsorption was obtained to be 252.2 mg/g, which confirms the synergistic effects of CZ root powder and MnFe2O4/g-C3N4 in enhancing overall adsorption capacity and efficiency.

The adsorption process was characterized and optimized, showing high removal efficiencies for Pb(II) under various conditions. Kinetic studies revealed that the adsorption process followed a pseudo-second-order model with high correlation. Isotherm studies showed that the Freundlich model best described the adsorption behavior, implying multilayer adsorption

on a heterogeneous surface, and indicating physisorption interactions, according to n values. Additionally, thermodynamic analyses confirmed that the adsorption process was endothermic and spontaneous, further validating the nanosorbent's efficiency.

To further improve the applicability of the study, XGBoost tuned using the Artificial Rabbits Optimization (ARO) algorithm was employed to model and predict the adsorption efficiency of Pb(II) on the nanosorbent. The model achieved a test set MSE of 0.358, with an R^2 value of 0.95, demonstrating strong predictive performance within the studied dataset. However, its generalization to broader experimental conditions remains to be validated with larger and more diverse data. Thus, while the integration of machine learning modeling shows promise for enhancing the reliability and scalability of adsorption studies, further work is required before confirming its applicability to practical water treatment systems.

Author Contribution Saba Madadgar: Writing – original draft, Methodology, Investigation, Formal analysis, Faramarz Doulati Ardejani: Writing – review & editing, Methodology, Conceptualization. Zohreh Boroumand: Writing – review & editing, Investigation, Formal analysis. Christopher Butscher: Writing – review & editing, Reza Taherdangkoo: Writing – review & editing, Methodology, Data Analysis.

Funding Open Access funding enabled and organized by Projekt DEAL.

Data Availability Data are available upon reasonable request.

Declarations

Ethics Approval and Consent to Participate Not applicable.

Consent for Publication All authors have consented to the publication of this work.

Competing interests The authors declare no competing interests.

Open Access This article is licensed under a Creative Commons Attribution 4.0 International License, which permits use, sharing, adaptation, distribution and reproduction in any medium or format, as long as you give appropriate credit to the original author(s) and the source, provide a link to the Creative Commons licence, and indicate if changes were made. The images or other third party material in this article are included in the article's Creative Commons licence, unless indicated otherwise in a credit line to the material. If material is not included in the article's Creative Commons licence and your intended use is not permitted by statutory regulation or exceeds the permitted use, you will need to obtain permission directly from the copyright holder. To view a copy of this licence, visit http://creativecommons.org/licenses/by/4.0/.

References

Abdel-Wahed, M. S., El-Kalliny, A. S., Badawy, M. I., Attia, M. S., & Gad-Allah, T. A. (2020). Core double-shell MnFe2O4@ rGO@ TiO2 superparamagnetic photocatalyst for wastewater treatment under solar light. *Chemical Engineering Journal, 382*, 122936.

AbuMousa, R. A., Khezami, L., Ismail, M., Ben Aissa, M. A., Modwi, A., & Bououdina, M. (2022). Efficient mesoporous MgO/g-C3N4 for heavy metal uptake: Modeling process and adsorption mechanism. *Nanomaterials (Basel), 12*(22), 3945.

Adeleke, O. A., Saphira, M. R., Daud, Z., Ismail, N., Ahsan, A., Ab Aziz, N. A., ... & Hijab, M. (2019). Locally derived activated carbon from domestic, agricultural and industrial wastes for the treatment of palm oil mill effluent. In Nanotechnology in water and wastewater treatment (pp. 35–62). Elsevier.

Ali, R. M., Hamad, H. A., Hussein, M. M., & Malash, G. F. (2016). Potential of using green adsorbent of heavy metal removal from aqueous solutions: Adsorption kinetics, isotherm, thermodynamic, mechanism and economic analysis. *Ecological Engineering, 91*, 317–332.

Alkherraz, A. M., Ali, A. K., & Elsherif, K. M. (2020). Removal of Pb (II), Zn (II), Cu (II) and Cd (II) from aqueous solutions by adsorption onto olive branches activated carbon: Equilibrium and thermodynamic studies. *Chemistry International, 6*(1), 11–20.

Al-Rashdi, B., Tizaoui, C., & Hilal, N. (2012). Copper removal from aqueous solutions using nano-scale diboron trioxide/titanium dioxide (B2O3/TiO2) adsorbent. *Chemical Engineering Journal, 183*, 294–302.

Amulya, M. S., Nagaswarupa, H. P., Kumar, M. A., Ravikumar, C. R., & Kusuma, K. B. (2021). Sonochemical synthesis of MnFe2O4 nanoparticles and their electrochemical and photocatalytic properties. *Journal of Physics and Chemistry of Solids, 148*, 109661.

Asadi, R., Abdollahi, H., Gharabaghi, M., & Boroumand, Z. (2020a). Effective removal of Zn (II) ions from aqueous solution by the magnetic MnFe2O4 and CoFe2O4 spinel ferrite nanoparticles with focuses on synthesis, characterization, adsorption, and desorption. *Advanced Powder Technology, 31*, 1480–1489.

Asadi, R., Abdollahi, H., Gharabaghi, M., & Boroumand, Z. (2020b). Effective removal of Zn (II) ions from aqueous solution by the magnetic MnFe2O4 and CoFe2O4 spinel ferrite nanoparticles with focuses on synthesis, characterization, adsorption, and desorption. *Advanced Powder Technology, 31*(4), 1480–1489.

Ayawei, N., Ekubo, A. T., Wankasi, D., & Dikio, E. D. (2015). Adsorption of Congo red by Ni/Al-CO3: Equilibrium, thermodynamic and kinetic studies. *Oriental Journal of Chemistry, 31*(3), 1307.

Badruddoza, A. Z. M., Shawon, Z. B. Z., Tay, W. J. D., Hidajat, K., & Uddin, M. S. (2013). Fe3O4/cyclodextrin polymer nanocomposites for selective heavy metals removal from industrial wastewater. *Carbohydrate Polymers, 91*(1), 322–332.

Bai, M. T., & Venkateswarlu, P. (2018). Fixed bed and batch studies on biosorption of lead using *Sargassum tenerrimum* powder: Characterization, kinetics and thermodynamics. *Materials Today: Proceedings, 5*(9), 18024–18037.

Baig, M. M., Yousuf, M. A., Agboola, P. O., Khan, M. A., Shakir, I., & Warsi, M. F. (2019). Optimization of different wet chemical routes and phase evolution studies of MnFe2O4 nanoparticles. *Ceramics International, 45*, 12682–12690. https://doi.org/10.1016/j.ceramint.2019.03.114

Bakhtiari, N., & Azizian, S. (2015). Adsorption of copper ion from aqueous solution by nanoporous MOF-5: A kinetic and equilibrium study. *Journal of Molecular Liquids, 206*, 114–118.

Bayuo, J., Rwiza, M. J., Choi, J. W., Mtei, K. M., Hosseini-Bandegharaei, A., & Sillanpää, M. (2024). Adsorption and desorption processes of toxic heavy metals, regeneration and reusability of spent adsorbents: Economic and environmental sustainability approach. *Advances in Colloid and Interface Science*. https://doi.org/10.1016/j.cis.2024.103196

Bora, T., & Dutta, J. (2014). Applications of nanotechnology in wastewater treatment—A review. *Journal of Nanoscience and Nanotechnology, 14*(1), 613–626.

Briffa, J., Sinagra, E., & Blundell, R. (2020). Heavy metal pollution in the environment and their toxicological effects on humans. *Heliyon, 6*, e04691. https://doi.org/10.1016/j.heliyon.2020.e04691

Chen, T., & Guestrin, C. (2016, August). Xgboost: A scalable tree boosting system. In Proceedings of the 22nd international conference on knowledge discovery and data mining (pp. 785–794).

Choumane, R., & Peulon, S. (2022). Innovative electrochemical process for a total removal and/or separation of soluble heavy metals. *Journal of Environmental Chemical Engineering, 10*(6), 108607.

Danh, L. T., Truong, P., Mammucari, R., Tran, T., & Foster, N. (2009). Vetiver grass, *Vetiveria zizanioides*: A choice plant for phytoremediation of heavy metals and organic wastes. *International Journal of Phytoremediation, 11*(8), 664–691.

Das, C., Singh, S., Bhakta, S., Mishra, P., & Biswas, G. (2022). Bio-modified magnetic nanoparticles with *Terminalia arjuna* bark extract for the removal of methylene blue and lead (II) from simulated wastewater. *Chemosphere, 291*, 132673.

Davarnejad, R., Shoaie, A., Karimi Dastnayi, Z., & Chehreh, M. (2020). Investigation of affecting parameters on the adsorption of lead (II) from aqueous solutions on henna powdered leaves. *Iranian Journal of Chemistry and Chemical Engineering (IJCCE), 39*(2), 181–189.

Doulati Ardejani, F., Badii, K. H., Limaee, N. Y., Shafaei, S. Z., & Mirhabibi, A. R. (2008). Adsorption of Direct Red 80 dye from aqueous solution onto almond shells: Effect of pH, initial concentration and shell type. *Journal of hazardous materials, 151*(2–3), 730–737.

Dubinin, M. M. (1947). The equation of the characteristic curve of activated charcoal. In *Dokl. Akad. Nauk. SSSR.* (Vol. 55, pp. 327–329).

Ekramul Mahmud, H. N. M., Obidul Huq, A. K., & Yahya, R. B. (2016). The Removal of Heavy Metal Ions from Wastewater/Aqueous Solution Using Polypyrrole-Based Adsorbents: A Review. *RSC Advances, 6*, 14778–14791. https://doi.org/10.1039/c5ra24358k

Eyvazi, B., Jamshidi-Zanjani, A., & Darban, A. K. (2020a). Synthesis of nano-magnetic MnFe2O4 to remove Cr(III) and Cr(VI) from aqueous solution: A comprehensive study. *Environmental Pollution, 265*, 113685. https://doi.org/10.1016/j.envpol.2019.113685

Eyvazi, B., Jamshidi-Zanjani, A., & Darban, A. K. (2020b). Synthesis of nano-magnetic MnFe2O4 to remove Cr (III) and Cr (VI) from aqueous solution: A comprehensive study. *Environmental Pollution, 265*, 113685.

Freundlich, H. (1907). On adsorption in solutions. *Journal of Physical Chemistry, 57*(1), 385–470.

Fu, F., Dionysiou, D. D., & Liu, H. (2014). The use of zero-valent iron for groundwater remediation and wastewater treatment: A review. *Journal of Hazardous Materials, 267*, 194–205.

Fuat, G., & Cumali, Y. (2021). Synthesis, characterization, and lead (II) sorption performance of a new magnetic separable composite: MnFe2O4@ wild plants-derived biochar. *Journal of Environmental Chemical Engineering, 9*(1), 104567.

Ghobadi, M., Gharabaghi, M., Abdollahi, H., Boroumand, Z., & Moradian, M. (2018). MnFe2O4-graphene oxide magnetic nanoparticles as a high-performance adsorbent for rare earth elements: Synthesis, isotherms, kinetics, thermodynamics and desorption. *Journal of Hazardous Materials, 351*, 308–316.

Goyal, P., Tiwary, C. S., & Misra, S. K. (2021). Ion exchange based approach for rapid and selective Pb (II) removal using iron oxide decorated metal organic framework hybrid. *Journal of Environmental Management, 277*, 111469.

Greenwood, N. N., & Earnshaw, A. (2012). *Chemistry of the Elements*. Elsevier.

Greluk, M., & Hubicki, Z. (2010). Kinetics, isotherm and thermodynamic studies of Reactive Black 5 removal by acid acrylic resins. *Chemical Engineering Journal, 162*(3), 919–926.

Gupta, V. K., Agarwal, S., & Saleh, T. A. (2011). Synthesis and characterization of alumina-coated carbon nanotubes and their application for lead removal. *Journal of Hazardous Materials, 185*(1), 17–23.

Hassan, M. R., & Aly, M. I. (2021). Magnetically synthesized MnFe2O4 nanoparticles as an effective adsorbent for lead ions removal from an aqueous solution. *Journal of Water Supply: Research and Technology-Aqua, 70*(6), 901–920.

Hu, J., Lo, I. M. C., & Chen, G. (2007). Comparative study of various magnetic nanoparticles for Cr (VI) removal. *Separation and Purification Technology, 56*(3), 249–256. https://doi.org/10.1016/J.SEPPUR.2007.02.009

Jiang, W., Yang, S., Sun, X., Lu, W., Jiang, D., Xu, L., Xu, H., Gao, B., Ma, M., & Cao, F. (2018). Quercetin-coated Fe 3 O 4 nanoparticle sensors based on low-field NMR for determination and removal of Pb 2+ and Cu 2+ in biological samples. *Analytical Methods, 10*(21), 2494–2502.

Kefeni, K. K., Mamba, B. B., & Msagati, T. A. (2017). Application of spinel ferrite nanoparticles in water and wastewater treatment: A review. *Separation and Purification Technology, 188*, 399–422.

Khodakarami, M., & Bagheri, M. (2021). Recent advances in synthesis and application of polymer nanocomposites for water and wastewater treatment. *Journal of Cleaner Production, 296*, 126404.

Kogularasu, S., Akilarasan, M., Chen, S. M., Elaiyappillai, E., Johnson, P. M., Chen, T. W., Al-Hemaid, F. M. A., Ali, M. A., & Elshikh, M. S. (2018). A comparative study on conventionally prepared MnFe2O4 nanospheres and template-synthesized novel MnFe2O4 nano-agglomerates as the electrodes for biosensing of mercury contaminations and supercapacitor applications. *Electrochimica Acta, 290*, 533–543. https://doi.org/10.1016/j.electacta.2018.09.028

Koizumi, M., et al. (2014). Graphene oxide-MnFe2O4 magnetic nanohybrids for efficient removal of lead and arsenic from water. *ACS Applied Materials & Interfaces, 6*(20), 20144–20153.

Kooti, G., Dabir, B., Butscher, C., & Taherdangkoo, R. (2024a). A constrained machine learning surrogate model to predict the distribution of water-in-oil emulsions in electrostatic fields. *Scientific Reports, 14*(1), 11142.

Kooti, G., Taherdangkoo, R., Chen, C., Sergeev, N., Doulati Ardejani, F., Meng, T., & Butscher, C. (2024b). Machine learning prediction of methane, ethane, and propane solubility in pure water and electrolyte solutions: Implications for stray gas migration modeling. *Acta Geochimica*. https://doi.org/10.1007/s11631-024-00680-8

Langmuir, I. (1916). The constitution and fundamental properties of solids and liquids. Part I. Solids. *Journal of the American Chemical Society, 38*(11), 2221–2295.

Li, Z., Gao, K., Han, G., Wang, R., Li, H., Zhao, X. S., & Guo, P. (2015). Solvothermal synthesis of MnFe2O4 colloidal nanocrystal assemblies and their magnetic and electrocatalytic properties. *New Journal of Chemistry, 39*, 361–368. https://doi.org/10.1039/C4NJ01466A

Lin, M., Huang, H., Liu, Z., Liu, Y., Ge, J., & Fang, Y. (2013). Growth–dissolution–regrowth transitions of Fe3O4 nanoparticles as building blocks for 3D magnetic nanoparticle clusters under hydrothermal conditions. *Langmuir, 29*(49), 15433–15441.

Liu, P., Rao, D., Zou, L., Teng, Y., & Yu, H. (2021). Capacity and potential mechanisms of Cd (II) adsorption from aqueous solution by blue algae-derived biochars. *Science of the Total Environment, 767*, 145447.

Madadgar, S., Doulati Ardejani, F., Boroumand, Z., Sadeghpour, H., Taherdangkoo, R., & Butscher, C. (2023). Biosorption of aqueous Pb (II), Co (II), Cd (II) and Ni (II) ions from Sungun copper mine wastewater by *Chrysopogon zizanioides* root powder. *Minerals, 13*(1), 106.

Mandal, S., Calderon, J., Marpu, S. B., Omary, M. A., & Shi, S. Q. (2021). Mesoporous activated carbon as a green adsorbent for the removal of heavy metals and Congo red: Characterization, adsorption kinetics, and isotherm studies. *Journal of Contaminant Hydrology, 243*, 103869.

Marcelo, L. R., de Gois, J. S., da Silva, A. A., & Cesar, D. V. (2021). Synthesis of iron-based magnetic nanocomposites and applications in adsorption processes for water treatment: A review. *Environmental Chemistry Letters, 19*(2), 1229–1274.

Maret, W. (2016). The metals in the biological periodic system of the elements: Concepts and conjectures. *International Journal of Molecular Sciences, 17*, 1–8. https://doi.org/10.3390/ijms17010066

Massoudinejad, M., Ghaderpoori, M., Shahsavani, A., Jafari, A., Kamarehie, B., Ghaderpoury, A., & Amini, M. M. (2018). Ethylenediamine-functionalized cubic ZIF-8 for arsenic adsorption from aqueous solution: Modeling, isotherms, kinetics and thermodynamics. *Journal of Molecular Liquids, 255*, 263–268.

Mohan, D., & Pittman, C. U., Jr. (2007). Arsenic removal from water/wastewater using adsorbents—a critical review. *Journal of Hazardous Materials, 142*(1–2), 1–53.

Momčilović, M., Purenović, M., Bojić, A., Zarubica, A., & Ranđelović, M. (2011). Removal of lead (II) ions from aqueous solutions by adsorption onto pine cone activated carbon. *Desalination, 276*(1–3), 53–59.

Morosanu, I., Teodosiu, C., Paduraru, C., Ibanescu, D., & Tofan, L. (2017). Biosorption of lead ions from aqueous effluents by rapeseed biomass. *New Biotechnology, 39*, 110–124.

Mortazavi, B., Shojaei, F., Shahrokhi, M., Azizi, M., Rabczuk, T., Shapeev, A. V., & Zhuang, X. (2020). Nanoporous C3N4, C3N5 and C3N6 nanosheets; Novel strong semiconductors with low thermal conductivities and appealing optical/electronic properties. *Carbon, 167*, 40–50.

Mulungulungu, G. A., Mao, T., & Han, K. (2021). Efficient removal of high-concentration copper ions from wastewater via 2D g-C3N4 photocatalytic membrane filtration. *Colloids and Surfaces a: Physicochemical and Engineering Aspects, 623*, 126714.

Netpradit, S., Thiravetyan, P., & Towprayoon, S. (2003). Application of 'waste'metal hydroxide sludge for adsorption of azo reactive dyes. *Water Research, 37*(4), 763–772.

Niu, Z., Zhang, S., Ma, M., Wang, Z., Zhao, H., & Wang, Y. (2019). Synthesis of novel waste batteries-sawdust-based adsorbent via a two-stage activation method for Pb 2+ removal. *Environmental Science and Pollution Research, 26*, 4730–4745.

Nodeh, H. R., & Sereshti, H. (2016). Synthesis of magnetic graphene oxide doped with strontium titanium trioxide nanoparticles as a nanocomposite for the removal of antibiotics from aqueous media. *RSC Advances, 6*(92), 89953–89965.

Obiri-Nyarko, F., Grajales-Mesa, S. J., & Malina, G. (2014). An overview of permeable reactive barriers for in situ sustainable groundwater remediation. *Chemosphere, 111*, 243–259.

Olya, M. E., Pirkarami, A., & Mirzaie, M. (2013). Adsorption of an azo dye in an aqueous solution using hydroxyl-terminated polybutadiene (HTPB). *Chemosphere, 91*, 935–940. https://doi.org/10.1016/j.chemosphere.2013.01.108

Ouma, I. L., Naidoo, E. B., & Ofomaja, A. E. (2018). Thermodynamic, kinetic and spectroscopic investigation of arsenite adsorption mechanism on pine cone-magnetite composite. *Journal of Environmental Chemical Engineering, 6*(4), 5409–5419.

Paul, S., Bera, D., Chattopadhyay, P., & Ray, L. (2006). Biosorption of Pb (II) by *Bacillus cereus* M1 16 immobilized in calcium alginate gel. *Journal of Hazardous Substance Research, 5*(1), 2.

Peng, H., & Guo, J. (2020). Removal of chromium from wastewater by membrane filtration, chemical precipitation, ion exchange, adsorption electrocoagulation, electrochemical reduction, electrodialysis, electrodeionization, photocatalysis and nanotechnology: A review. *Environmental Chemistry Letters, 18*(6), 2055–2068.

Pezeshki, H., Hashemi, M., & Rajabi, S. (2023). Removal of arsenic as a potentially toxic element from drinking water by filtration: A mini review of nanofiltration and reverse osmosis techniques. *Heliyon*. https://doi.org/10.1016/j.heliyon.2023.e14246

Rajput, S., Pittman, C. U., Jr., & Mohan, D. (2016). Magnetic magnetite (Fe3O4) nanoparticle synthesis and applications for lead (Pb2+) and chromium (Cr6+) removal from water. *Journal of Colloid and Interface Science, 468*, 334–346.

Ramalingam, G., Perumal, N., Priya, A. K., & Rajendran, S. (2022). A review of graphene-based semiconductors for photocatalytic degradation of pollutants in wastewater. *Chemosphere, 300*, 134391.

Rathi, V., Panneerselvam, A., & Sathiyapriya, R. (2020). Surface decoration of MnWO4 nanoparticles with g-C3N4 nanosheets to build hetero-structure and its structural, optical and enhanced visible light photocatalytic activity. *Journal of Materials Science: Materials in Electronics, 31*(17), 14823–14837.

Sadeghpour, H., Shafaei, S. Z., Ardejani, F. D., Boroumand, Z., Darestani, P. A., Madadgar, S., & Hasani, S. (2023a). Arsenic removal by highly efficient MnFe2O4/TiO2/g-C3N4 and MnFe2O4/TiO2/GO adsorbents from a groundwater sample, Bardsir, Iran. *Environmental Nanotechnology, Monitoring & Management, 20*, 100821.

Sadeghpour, H., Tonkaboni, S., Ziaedin, S., Doulati Ardejani, F., Boroumand, Z., Darestani, P., Madadgar, S., & Hasani, S. (2023b). Arsenic removal by highly efficient MnFe2O4/TiO2/g-C3N4 and MnFe2O4/TiO2/GO adsorbents from a groundwater sample, Bardsir, Iran. *Environmental Nanotechnology, Monitoring & Management., 20*, 100821. https://doi.org/10.1016/j.enmm.2023.100821

Saeidpour, S., Khoshnevisan, B., & Boroumand, Z. (2022). Synthesis and characterization of a g-C3N4/TiO2-ZnO nanostructure for photocatalytic degradation of methylene blue. *Nano Futures, 6*(3), 035001.

Sahmoune, M. N. (2019). Evaluation of thermodynamic parameters for adsorption of heavy metals by green adsorbents. *Environmental Chemistry Letters, 17*(2), 697–704.

Sezgin, N., Yalcin, A., Koseog˘lu, Y., (2015). MnFe2O4 nano spinels as potential sorbent for adsorption of chromium from industrial wastewater, *Desalination and Water Treatment 57*, 16495–16505. https://doi.org/10.1080/19443994.2015.1088808

Sharahi, F. J., & Shahbazi, A. (2017). Melamine-based dendrimer amine-modified magnetic nanoparticles as an efficient Pb (II) adsorbent for wastewater treatment: Adsorption optimization by response surface methodology. *Chemosphere, 189*, 291–300.

Shen, C., Chen, C., Wen, T., Zhao, Z., Wang, X., & Xu, A. (2015). Superior adsorption capacity of g-C3N4 for heavy metal ions from aqueous solutions. *Journal of Colloid and Interface Science, 456*, 7–14.

Singh, G., & Chandra, S. (2018). Electrochemical performance of MnFe2O4 nanoferrites synthesized using thermal decomposition method. *International Journal of Hydrogen Energy, 43*, 4058–4066. https://doi.org/10.1016/j.ijhydene.2017.08.181

Socrates, G. (2004). *Infrared and Raman characteristic group frequencies: Tables and charts*. John Wiley & Sons.

Soliman, N. K., & Moustafa, A. F. (2020). Industrial solid waste for heavy metals adsorption features and challenges; A review. *Journal of Materials Research and Technology, 9*(5), 10235–10253.

Stuart, B. H. (2004). *Infrared spectroscopy: Fundamentals and applications*. John Wiley & Sons.

Taherdangkoo, R., Nagel, T., Chen, C., Mollaali, M., Ghasabeh, M., Cuisinier, O., Abdallah, A., & Butscher, C. (2024). Modeling unsaturated hydraulic conductivity of compacted bentonite using a constrained CatBoost with bootstrap analysis. *Applied Clay Science, 260*, 107530.

Takeno, N. (2005). Atlas of eh-pH diagrams. *Geological Survey of Japan Open File Report, 419*(102), 285.

Taleb, M. A., Kumar, R., Barakat, M. A., Almeelbi, T., Seliem, M. K., & Ahmad, A. (2024). Recent advances in heavy metals uptake by tailored silica-based adsorbents. *Science of the Total Environment, 955*, 177093.

Tang, Y., Chen, L., Wei, X., Yao, Q., & Li, T. (2013). Removal of lead ions from aqueous solution by the dried aquatic plant, *Lemna perpusilla* Torr. *Journal of Hazardous Materials, 244*, 603–612.

Thue, P. S., Sophia, A. C., Lima, E. C., Wamba, A. G., de Alencar, W. S., dos Reis, G. S., ... & Dias, S. L. (2018). Synthesis and characterization of a novel organic-inorganic hybrid clay adsorbent for the removal of acid red 1 and acid green 25 from aqueous solutions. Journal of Cleaner Production, 171, 30–44.

Titchou, F. E., Zazou, H., Afanga, H., El Gaayda, J., Akbour, R. A., & Hamdani, M. (2021). Removal of persistent organic pollutants (POPs) from water and wastewater by adsorption and electrocoagulation process. *Groundwater for Sustainable Development, 13*, 100575.

Truong, P. (1999). *Vetiver grass technology for mine rehabilitation* (Vol. 19). Bangkok: Office of the Royal Development Projects Board.

Ugwu, E. I., Tursunov, O., Kodirov, D., Shaker, L. M., Al-Amiery, A. A., Yangibaeva, I., & Shavkarov, F. (2020, December). Adsorption mechanisms for heavy metal removal using low cost adsorbents: A review. In IOP Conference Series: Earth and Environmental Science (Vol. 614, No. 1, p. 012166). IOP Publishing.

Velarde, L., Nabavi, M. S., Escalera, E., Antti, M. L., & Akhtar, F. (2023). Adsorption of heavy metals on natural zeolites: A review. *Chemosphere, 328*, 138508.

Wang, J., & Chen, C. (2009). Biosorbents for heavy metals removal and their future. *Biotechnology Advances, 27*(2), 195–226.

Wang, J., & Guo, X. (2020). Adsorption isotherm models: Classification, physical meaning, application and solving method. *Chemosphere, 258*, 127279.

Wang, L., Li, J., Jiang, Q., & Zhao, L. (2012). Water-soluble Fe 3 O 4 nanoparticles with high solubility for removal of heavy-metal ions from waste water. *Dalton Transactions, 41*(15), 4544–4551.

Wang, X., Liang, Y., An, W., Hu, J., Zhu, Y., & Cui, W. (2017). Removal of chromium (VI) by a self-regenerating and metal free g-C3N4/graphene hydrogel system via the synergy of adsorption and photo-catalysis under visible light. *Applied Catalysis b: Environmental, 219*, 53–62.

Wang, G., Zhao, D., Kou, F., Ouyang, Q., Chen, J., & Fang, Z. (2018). Removal of norfloxacin by surface fenton system (MnFe2O4/H2O2): Kinetics, mechanism and degradation pathway. *Chemical Engineering Journal, 351*, 747–755. https://doi.org/10.1016/j.cej.2018.06.033

Wang, W., Zhao, P., Hu, Y., & Zan, R. (2020). Application of weak magnetic field coupling with zero-valent iron for remediation of groundwater and wastewater: A review. *Journal of Cleaner Production, 262*, 121341.

Wang, R., Deng, L., Fan, X., Li, K., Lu, H., & Li, W. (2021). Removal of heavy metal ion cobalt (II) from wastewater via adsorption method using microcrystalline cellulose–magnesium hydroxide. *International Journal of Biological Macromolecules, 189*, 607–617.

Wang, L., Cao, Q., Zhang, Z., Mirjalili, S., & Zhao, W. (2022). Artificial rabbits optimization: A new bio-inspired meta-heuristic algorithm for solving engineering optimization problems. *Engineering Applications of Artificial Intelligence, 114*, 105082.

World Health Organization, and W. Guidelines for Drinking-Water Quality; 2004.

Xiang, Z., Tang, N., Jin, X., & Gao, W. (2022). Fabrications and applications of hemicellulose-based bio-adsorbents. *Carbohydrate Polymers, 278*, 118945.

Xie, D., et al. (2022). Efficient RhB degradation using MnFe2O4/g-C3N4 composites under visible light irradiation. *Optical Materials, 124*, 111965. https://doi.org/10.1016/J.OPTMAT.2021.111965

Xu, P., Zeng, G. M., Huang, D. L., Lai, C., Zhao, M. H., Wei, Z., Li, N. J., Huang, C., & Xie, G. X. (2012). Adsorption of Pb (II) by iron oxide nanoparticles immobilized *Phanerochaete chrysosporium*: Equilibrium, kinetic, thermodynamic and mechanisms analysis. *Chemical Engineering Journal, 203*, 423–431.

Xu, W.-H., Wang, L., Wang, J., Sheng, G.-P., Liu, J.-H., Yu, H.-Q., & Huang, X.-J. (2013). Superparamagnetic mesoporous ferrite nanocrystal clusters for efficient removal of arsenite from water. *CrstEngComm, 15*(39), 7895.

Yaashikaa, P. R., Kumar, P. S., Jeevanantham, S., & Saravanan, R. (2022). A review on bioremediation approach for heavy metal detoxification and accumulation in plants. *Environmental Pollution, 301*, 119035.

Yadava, K. P., Tyagi, B. S., & Singh, V. N. (1991). Effect of temperature on the removal of lead (II) by adsorption on China clay and wollastonite. *Journal of Chemical Technology & Biotechnology, 51*(1), 47–60.

Younas, F., Mustafa, A., Ur, Z., Farooqi, R., Wang, X., Younas, S., Mohy-ud-din, W., Hameed, M. A., Abrar, M. M., Maitlo, A. A., et al. (2021). Current and emerging adsorbent technologies for wastewater treatment: Trends, limitations, and environmental implications. *Water (Basel), 13*, 1–25.

Zhang, C., Jin, C., Teng, G., Gu, Y., & Ma, W. (2019a). Controllable synthesis of hollow MnFe2O4 by self-etching and its application in high-performance anode for lithium-ion batteries. *Chemical Engineering Journal, 365*, 121–131. https://doi.org/10.1016/j.cej.2019.02.004

Zhang, Y., Ni, S., Wang, X., Zhang, W., Lagerquist, L., Qin, M., Willför, S., Xu, C., & Fatehi, P. (2019b). Ultrafast adsorption of heavy metal ions onto functionalized lignin-based hybrid magnetic nanoparticles. *Chemical Engineering Journal, 372*, 82–91.

Publisher's Note Springer Nature remains neutral with regard to jurisdictional claims in published maps and institutional affiliations.